Total Generalized Variation regularization for multi-modal electron tomography

Richard Huber,[*,†] Georg Haberfehlner,[*,‡,¶] Martin Holler,[*,†,§] Gerald Kothleitner,[*,‡,¶] and Kristian Bredies[*,†]

†*Institute for Mathematics and Scientific Computing, University of Graz, Heinrichstraße 36, A-8010 Graz, Austria*

‡*Institute of Electron Microscopy and Nanoanalysis, Graz University of Technology, Steyrergasse 17, 8010 Graz, Austria*

¶*Graz Centre for Electron Microscopy, Steyrergasse 17, 8010 Graz, Austria*

§*Centre de Mathmatiques Appliquées, École Polytechnique, 91128 Palaiseau Cedex, France.*

E-mail: richard.huber@uni-graz.at; georg.haberfehlner@felmi-zfe.at; martin.holler@uni-graz.at; gerald.kothleitner@felmi-zfe.at; kristian.bredies@uni-graz.at

Supporting Information

Effects of data inconsistencies

Here we show in Figure 1 on a simple example which type of data inconsistencies typically occur and what their effects on the reconstruction are. Supporting Figure 1a shows the original data and its reconstruction.

Intensity fluctuations. In electron tomography data one might observe intensity fluctuations between different tilt angles. There are two main sources for this effects: Partial shadowing of the detector, and residual diffraction contrast. Partial detector shadowing is present in our case at very large tilt angles, as we used a conventional TEM grid, where a part of the scattered electrons may hit the (tilted) TEM grid. HAADF STEM as well as EELS and EDXS are TEM techniques with low contributions of diffraction contrast, which is why they are the principal techniques used for electron tomography of crystalline samples. However some contribution of diffraction contrast can still be present, which leads to brightness fluctuations depending on tilt angles, and in extreme cases may even lead to contrast inversion. Both these effects are depicted in Supporting Figure 1b, where the intensities in the sinogram are fluctuating, and the topmost and bottommost projections (corresponding to large tilt angles) are darker. This can lead to additive artifacts appearing inside and outside the observed object.

Non-zero basevalue & Gaussian noise. Often, the data get rescaled in the line of procession before reconstruction starts, however, for the Radon transform it is imperative that the basevalue (which correspond to no density) has the value 0. Also, such data suffers from thermic (Gaussian) noise due to the electronics of the detector. Though generally much lower than the Poisson noise, Gaussian noise is particularly relevant in points with no density, which is not consistent to the noise model, see Supporting Figure 1c. Therefore, the reconstruction scheme must insert additional mass to make up for the non-zero basevalue and noise outside the object, resulting in noise and halo artifacts occurring.

Misalignment. Misalignment of the tilt series can be an issue in electron tomography. One must also be wary, that the alignment of the projection is correct, meaning that each projection is centered with respect to a common tilt axis. An example for a severely misaligned sinogram is shown in Supporting Figure 1d along with its reconstruction. An non-correct alignment leads to blurring of the image, and artifacts outside the object as one can see in the reconstruction. For good alignment we used center of mass and common-line

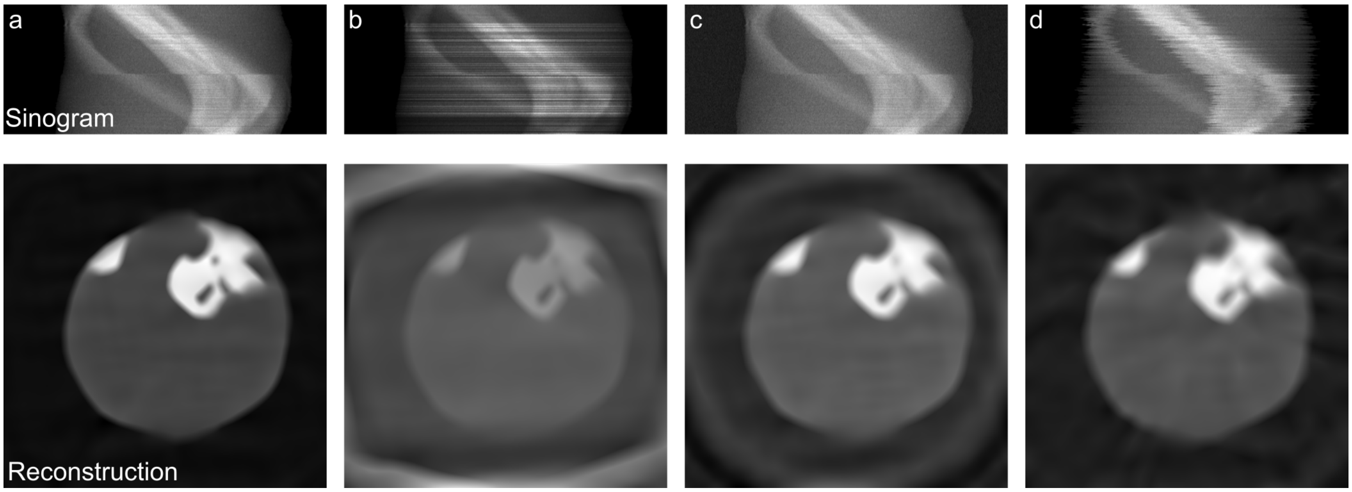

Figure 1: Experiments on effects of inconsistent data. (a) original, (b) intensity fluctuations, (c) non-zero basevalue, (d) misalignment. The top row shows the sinograms and the bottom row the corresponding reconstructions.

alignment methods as described in the section *Data preprocessing*.

We note that although each of these artifacts appearing without preprocessing might not be very significant, when all the described problems occur at once, they further amplify one another.

Table 1: Parameter choice for the reconstructions of the phantom data presented in the paper. For SIRT we provide the number of iterations and for TV and TGV regularization the weights of the data discrepancies of the different channels.

	SIRT	TV Uncorr. 2D	TV Coupl. 2D	TV Uncorr. 3D	TV Coupl. 3D
HAADF	50	0.5	0.5	0.2	0.2
Ytterbium	25	5.5 10^{-4}	1 10^{-4}	8 10^{-4}	5 10^{-4}
Aluminum	25	20 10^{-4}	15 10^{-4}	60 10^{-4}	40 10^{-4}
Silicon	25	5.5 10^{-4}	1.5 10^{-4}	10 10^{-4}	5 10^{-4}

	TGV Uncorr. 2D	TGV Coupl. 2D	TGV Uncorr. 3D	TGV Coupl. 3D
HAADF	0.3	0.3	0.2	0.2
Ytterbium	2.5 10^{-4}	2 10^{-4}	7.5 10^{-4}	5 10^{-4}
Aluminum	25 10^{-4}	10 10^{-4}	60 10^{-4}	40 10^{-4}
Silicon	5 10^{-4}	2.5 10^{-4}	10 10^{-4}	5 10^{-4}

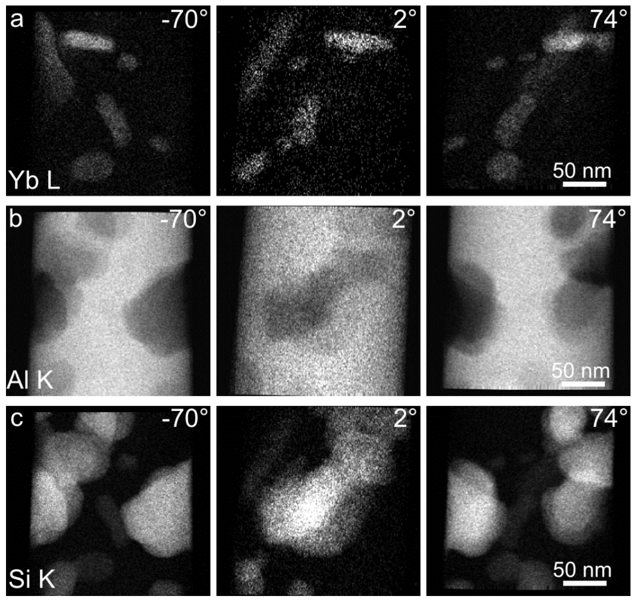

Figure 2: Projections of EDXS data for the experimental data discussed in the section *Experimental reconstruction*: (a) Yb L-lines, (b) Al K-lines, (c) Si K-lines under 3 different viewing angles.

Extension to limited angle tomography

Here we provide further experiments and automatic parameter choice strategies for the situation of different, limited angle measurements. Regarding the parameter choice for varying, limited angle measurements, we have adopted the following heuristic: Given a set of parameters that are well suited for an experiment with a certain number of angle measurements, for a second measurement define λ to be the fraction of available angle measurements for the new measurement compared to the original one, e.g., $\lambda = 1/2$ would mean that only half as many measurements are available. Since reduced measurements reduce the overall cost of the data term by the same factor, we compensate for that by rescaling all parameters μ^c with the factor $1/\lambda$. Figure 4 shows results using this strategy with 3D TGV regularization for different, limited angle measurements, where the experiment and parameter setting of Figure 3 of the paper were taken as reference setting. As can be observed, while reduced angle measurements naturally degrade image quality, the results

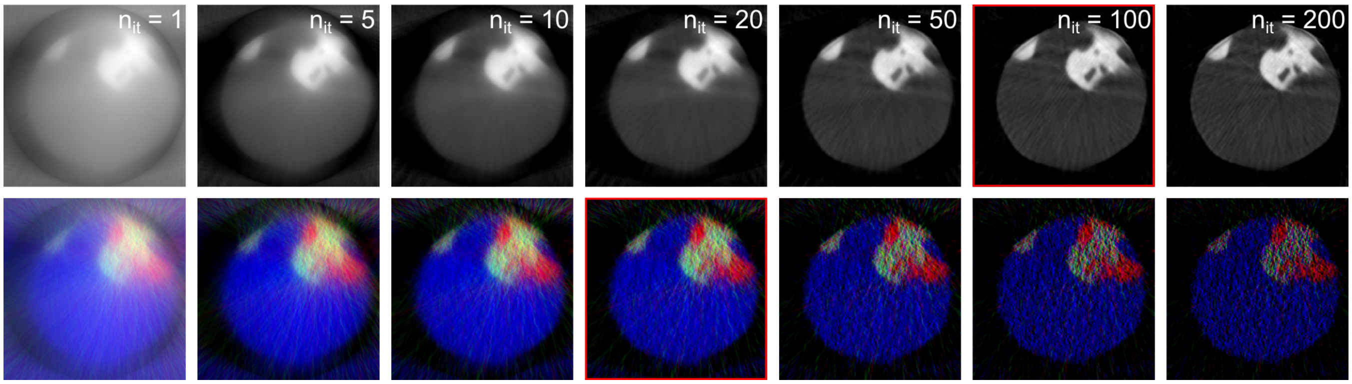

Figure 3: Comparison of different numbers of iterations for SIRT reconstructions of HAADF and EDXS data for the experimental data discussed in the section *Experimental reconstruction*. The chosen reconstructions are framed in red.

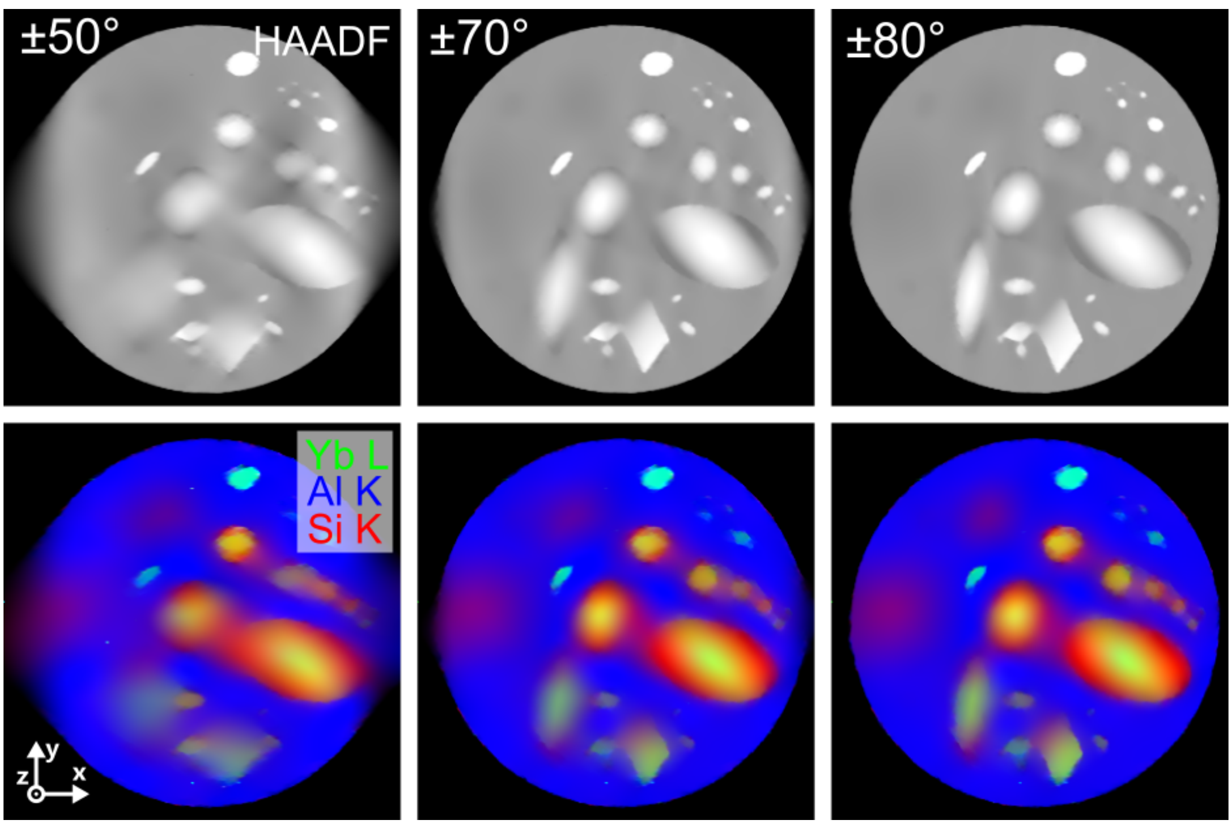

Figure 4: Effects of limited angles on reconstruction. Shows HAADF (upper row) and EDX (lower row) reconstructions with angle range ±50° ±70° and ±80° using 3-dimensional coupled TGV.

are still rather reasonable indicating that the proposed parameter adaption strategy is effective.

Quantitative analysis of experiments

In section "Reconstruction of phantom data" qualitative results for the phantom were shown, which we want to extent here with some quantitative analysis. To this aim, we have computed SIRT-, uncoupled 2D TV- and coupled 3D TGV reconstructions for the simulated data and 100 different noise realizations, using the parameters as described in Table 1. Figure 5 shows, for the three methods and the aluminum channel, the point-wise mean over all noise realizations, the point-wise difference of the mean to the ground truth and the pointwise standard deviation. It can be observed that TGV has a mean that is closest to the ground truth while at the same time also having the lowest standard deviation. This visual observation is confirmed by Table 2, showing lowest mean error and standard deviation for 3-dimensional coupled TGV. Here, mean error refers to the root of the squared sum of the point-wise difference between the mean and the ground truth for each method and the standard deviation is the root of the squared sum of the point-wise standard deviation.

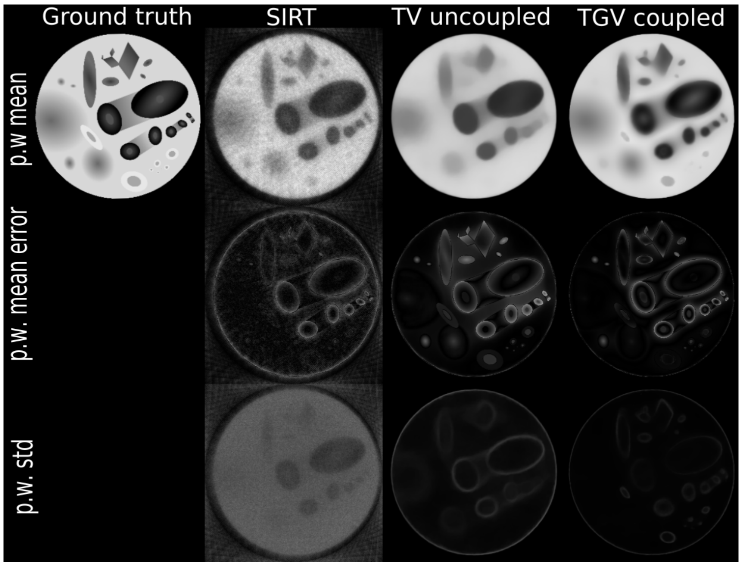

Figure 5: Mean and standard deviation maps for the aluminum channel over 100 different noise realizations.

	Mean error ± Std
SIRT	10.50 ± 24.43
TV	8.52 ± 4.93
TGV	6.073 ± 2.44

Table 2: Mean error ± standard deviation.

Computational evaluation of the Radon transform implementation

As described in the "Variational modeling" section, our algorithm uses a custom, GPU-based implementation of the discrete Radon transform. Here we provide a brief comparison of this implementation against the one of the Astra toolbox[1,2]. The first experiment concerns the numerical adjointness of the forward and adjoint operator. As mentioned in "Variational modeling", one advantage of our custom implementation is that the adjoint operator is the numerical adjoint, which is important for convergence of iterative algorithms. To evaluate this, we carried out the following experiment. Based on a simulated ground truth image, two different data, once with the Astra forward operator and once with our implementation, were generated. Then, a Landweber[3] reconstruction was carried out, using the Astra forward and backward operator for the Astra-generated data and our operators for the other one. As the convergence plot in Figure 6 shows, both methods converge well up to a certain accuracy but then convergence with the Astra operator slows down and saturates. We believe that this can be attributed to numerical errors due to the adjoint operator not being the numerical adjoint. As second experiment, Table 3 shows the computation time for 10^4 repetitions of the forward and backward transform using once our custom implementation and once the one of the Astra toolbox. As can be seen there, in this simple test our method performs comparable to the Astra implementation.

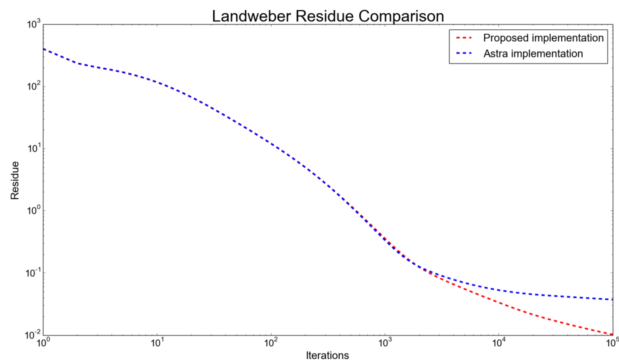

Figure 6: Residue of a Landweber reconstruction approach using either the Astra or the proposed implementations of the Radon transform and the backprojection for a single slice of the phantom data for aluminum with 305 × 305 pixels, 320 detectors and 100 angles equally distributed.

GPU	GeForce GTX 980		Nvidia Tesla K40c	
Implementation	Astra	Proposed	Astra	Proposed
Radon transform	24.34	24.02	44.05	38.02
Backprojection	28.64	2.26	47.60	7.57

Table 3: Computation time (in seconds) on two different GPUs for 10000 evaluations with the proposed GPU implementation and Astra GPU implementation on a single slice of phantom data for aluminum with 305 × 305 pixels, 320 detectors and 100 angles equally distributed.

References

1. Palenstijn, W. J.; Bédorf, J.; Sijbers, J.; Batenburg, K. J. A distributed ASTRA toolbox. *Advanced Structural and Chemical Imaging* **2016**, *2*, 19.

2. van Aarle, W.; Palenstijn, W. J.; Cant, J.; Janssens, E.; Bleichrodt, F.; Dabravolski, A.; Beenhouwer, J. D.; Batenburg, K. J.; Sijbers, J. Fast and flexible X-ray tomography using the ASTRA toolbox. *Opt. Express* **2016**, *24*, 25129–25147.

3. Landweber, L. An Iteration Formula for Fredholm Integral Equations of the First Kind. *American Journal of Mathematics* **1951**, *73*, 615–624.